The Report Committee for Matthew Scott Byrne
Certifies that this is the approved version of the following Report:

Acoustic Supercoupling with Compressibility-Near-Zero Effective Material Properties

APPROVED BY
SUPERVISING COMMITTEE:

Andrea Alù, Supervisor

Mark F. Hamilton, Co-Supervisor

Acoustic Supercoupling with Compressibility-Near-Zero Effective Material Properties

by

Matthew Scott Byrne

Report

Presented to the Faculty of the Graduate School of

The University of Texas at Austin

in Partial Fulfillment

of the Requirements

for the Degree of

Master of Science in Engineering

The University of Texas at Austin

May 2018

Dedication

To my parents for a lifetime of unwavering support and encouragement. To my girlfriend for always being there when I need her.

Acknowledgements

This report was largely inspired and supported by the guidance of my advisor, Professor Andrea Alù. I would like to thank him for his generous investment of time, as well as for encouragement and advice throughout my first two years of graduate study. He has served both as a model scientist and manager of our research group and I will proudly carry forward his example throughout my career.

I would also like to thank Professor Michael Haberman for helpful research discussions and for connecting me with laboratory resources at the Applied Research Lab at UT. Moreover, I must thank Professor Mark Hamilton for his exceptional dedication to teaching Physical Acoustics at UT Austin and for his generous availability during office hours throughout my time here.

I was very lucky to collaborate on this research with Dr. Hussein Esfahlani, and I thank him for his guidance, patience, and integrity while assisting me in developing analytical theory, building numerical simulations, scrutinizing results, and preparing my first academic publications. Additionally, special thanks is given to Matthew McDermott, who was an invaluable research assistant during our experimental investigations.

Much thanks are also owed to the following researchers for useful discussions related to this work (in alphabetical order): Dr. Anthony Bonomo, Dr. Ahmed Kord, Dr. Caleb Sieck, and Dr. Dimitrios Sounas.

In addition, I would like to thank all of my fellow students in the Alù Group for their friendship and support throughout my first two years in Austin. Finally, I must thank our administrative staff for their help in navigating hurdles along the way: Melanie Gulick, Karen Little, Apipol Piman, and Melody Singleton.

Abstract

Acoustic Supercoupling with Compressibility-Near-Zero Effective Material Properties

Matthew Scott Byrne, MSE

The University of Texas at Austin, 2018

Supervisor: Andrea Alù

Co-Supervisor: Mark Hamilton

Supercoupling is a widely-researched topic in wave engineering, which has been used to build coupling channels that can, in principle, support total transmission and complete phase uniformity, independent of the length of the channel. This has generally been accomplished by employing dispersion in media that display a near-zero index. In the field of acoustics, prior works have required the presence of periodic embedded resonators, such as membranes or Helmholtz resonators, in order to observe near-zero properties. Here we show, theoretically and experimentally, that supercoupling can occur in an acoustic channel without the presence of embedded resonators. A compressibility-near-zero (CNZ) acoustic channel was observed to show remarkable properties analogous to those found in electromagnetics. Furthermore, by employing higher-order modes, we demonstrate the realization of effective soft boundary conditions in air, which are exploited to produce uniform phase in the coupling channel. In the second chapter of this work, we show that these concepts can be extended to realize a novel acoustic power

divider, which permits the tunneling of acoustic power to an arbitrary number of output ports, where the phase shift with respect to the input signal can be selected to be either 0 or 180 degrees. We also present analytical and numerical models, which describe the behavior of the power divider, and conclude with an analysis that describes the limitations and trade-offs that occur due to losses as the device size is scaled.

Table of Contents

Chapter 1: Overview of Compressibility-Near-Zero Supercoupling[1]

INTRODUCTION

Over the past decade, much attention has been paid to near-zero-index metamaterials due their exceptional wave-manipulating properties [1]. These materials can be described by constitutive relations which are temporally and spatially decoupled due to the near-zero material parameters, leading to interesting scattering and propagation phenomena [2]. Although the majority of this research has been in the electromagnetic realm, regarding media with near-zero dielectric permittivity (epsilon-near-zero or ENZ)[2]-[9], near-zero magnetic permeability (mu-near-zero or MNZ)[10] or double-near-zero materials (epsilon-and-mu-near-zero or EMNZ) [11][12], recent attention has also been given to analogous phenomena in the fields of optics [13][14], plasmonics [15][16], photonics [17][18], and acoustics [19]-[23].

Remarkable properties for near-zero-index media have been proposed and experimentally validated. For instance, these metamaterials have been used for cloaking [24]-[25], improving the directivity of a radiating body [26]-[27], and supercoupling [3][24][28]-[29]. It was shown that supercoupling enables electromagnetic energy to be tunneled, regardless of a channels' arbitrary geometrical shape and bending, through narrow channels filled with permittivity-near-zero material [4]-[8] or through a wide intermediate channel filled with permeability-near-zero material [24]. Furthermore, transmission line theory was developed to aid in a more intuitive understanding of such

[1] Portions of this chapter are planned for publication as a part of a group effort. This work was completed with Hussein Esfahlani and myself as first co-authors, followed by Matthew McDermott and Andrea Alù as additional authors. Hussein Esfahlani initiated the research and developed most of the analytical theory. Hussein and I spent equal effort on the numerical simulations. I took the lead on the experimental measurements with the assistance of Matt McDermott. Andrea Alù supervised the research.

structures [9]. In another study, it was shown that ENZ supercoupling can be used to boost optical nonlinearities in plasmonic channels [16].

Following the path of electromagnetic near-zero-index materials, the physics of acoustic metamaterials with near-zero material properties has recently been studied. For example, a space-coiled structure was used to assess a density-near-zero material for acoustic tunneling [19]. Using a waveguide populated with transverse membranes and side holes, which exhibits density-and-compressibility-near-zero properties, an acoustic leaky-wave antenna with broadside radiation was achieved [20][21]. Additionally, a membrane-based acoustic metamaterial with a near-zero-density was proposed as an angular filter which only transmits a wave with a near-zero incident angle [22].

Furthermore, prior concepts employing near-zero index material properties were demonstrated to enable acoustic supercoupling. One approach theoretically showed that energy could be squeezed through ultranarrow acoustic channels, by employing a waveguide filled with arrays of transverse membranes [23]. However, challenges with visco-thermal loss and the accurate tuning of membrane resonances have prevented the practical realization of density-near-zero acoustic devices thus far. Additionally, a waveguide embedded with Helmholtz resonators in the form of low pass filters was shown to support compressibility-near-zero properties and uniform phase through an intermediate channel [30]. In the present work, a more geometrically simple and hence more practical acoustic system is proposed, which is uniquely shown to demonstrate supercoupling independent of the length, height, and arbitrary bending of the channel. In addition to experimental results, analytical and numerical models are provided for the design of compressibility-near-zero channels. Furthermore, we describe a theoretical methodology for designing such structures with “effective soft boundary conditions”. These boundary conditions provide a means to realize an acoustic waveguide that has a

first cut-off frequency at a value greater than 0 Hz, despite the presence of physically hard boundaries. This approach presents a more tractable acoustic supercoupling concept, which may establish new pathways for acoustic cloaking, acoustic sensing, and acoustic wave patterning.

RESULTS

Acoustic tunneling with varying boundary conditions

To study supercoupling and compressibility-near-zero properties in a simple waveguide geometry, we consider the proposed configuration of Fig. 1. In this configuration, we place a wide intermediate channel, with specific acoustic impedance Z_2 and cross-sectional area S_2, and sandwich it between two narrow input/output channels, each with specific acoustic impedance Z_1 and cross-sectional area S_1. We then feed the input waveguide at a frequency close to a cut-off frequency of the intermediate channel. Due to the emergence of cut-off in the acoustic waveguide, there will be propagation of a mode associated with that specific cut-off frequency and more importantly dispersion will occur near the cut-off frequency. Therefore, it is expected that the effective material properties of the intermediate waveguide (ρ_{eff2}, κ_{eff2}) become frequency-dependent and different from the material properties of the filling fluid at frequencies away from cut-off (ρ_{0_2} , κ_{0_2}). Here, ρ and κ are respectively the density and stiffness of the fluid. In the methods section, we analytically show that the proposed waveguide configuration of Fig. 1 with specific wall boundary arrangements can exhibit $\kappa_{eff\,2} \to \infty\,(C_{eff\,2} \to 0)$ when it is operated near its cut-off frequency (where C is defined as the compressibility of the fluid). We also show how this condition will lead to impedance matching and uniform phase, as observed in electromagnetic waveguides [8]. Here, we present the results of two

simple waveguide configurations that could lead to supercoupling, although other configurations may also be possible.

Parallel soft/hard boundary conditions

Let us consider the waveguide configuration of Fig. 1, in which all the walls are hard except for two parallel walls at $x = \{0, a\}$. As discussed and shown in the Methods section, such a waveguide exhibits its first non-trivial cut-off at a frequency that coincides with near-zero compressibility. Hence, it is expected that the acoustic wave will tunnel, with uniform phase and full transmission, when operated near its first non-trivial cut-off frequency.

To examine the aforementioned proposal, the cross-sectional areas of the input/output waveguides are kept fixed, while the dimensions of the channel are changed. Fig. 2a shows the transmission coefficients of the proposed configuration, having two parallel soft and two parallel hard boundaries, with varying channel lengths (L). For each length, the first peak corresponds to the tunneling frequency, which occurs near the cut-off frequency of the intermediate channel. The following peaks in the transmission coefficient are due to Fabry-Perot resonances. By increasing the length of the channel, the number of Fabry-Perot resonances increase for a fixed frequency spectrum, however the tunneling frequency remains unchanged and independent of the channel's length.

Fig. 2b presents the corresponding 2D phase profile in the channels at the tunneling frequencies. We observe completely uniform phase, independent of the length of the coupling channel. The phase is uniform for two reasons: 1) $S_1 \ll S_2$, which ensures that impedance matching between the input/output waveguides and the intermediate channel occurs very close to the cut-off frequency, and 2) the waveguide is

fed near the cut-off frequency of the first propagating mode, therefore no other modes can propagate and thus interfere with the phase pattern within the channel.

The importance of the $\frac{S_2}{S_1}$ ratio can be further explained by analysis of the transmission coefficients for channels with similar dimensions but varying heights. For example, the phase variation is $\approx \frac{\pi}{2}$ for an acoustic tunneling channel of length L = 400cm and height b = 8cm, but the phase change becomes flat and ≈ 0 for the same channel with a larger height, b = 40cm. This is explained by analytically studying the channel's acoustic impedance and phase velocity. By evaluating for the (1,0) mode

$$Z_z = \frac{\omega \rho_0}{S\sqrt{(\frac{\omega}{c_0})^2 - (\frac{\pi}{a})^2}} \quad (1)$$

It is clear that the denominator of this relation goes to zero near the cut-off frequency which can be expressed as

$$f_{mn}^c = \frac{c}{2\pi}\sqrt{(\frac{m\pi}{a})^2 + (\frac{n\pi}{b})^2} \quad (2)$$

with *m=1* and *n=0*, and the overall impedance value in Eq. 1 blows up. However, due to the very steep slope with respect to frequency, impedance matching should be satisfied in a close vicinity of the cut-off frequency to achieve very high phase velocity, thus ensuring constant phase through the channel. This can be achieved by increasing the $\frac{S_2}{S_1}$ ratio, which moves the frequency of matched impedance towards the cut-off frequency and leads to very large value of phase velocity.

Parallel hard/hard boundary conditions

We now turn to analysis of a supercoupling design with the intermediate channel consisting of all sound-hard boundary conditions, with air as the filling fluid. Given that $S_1 \ll S_2$, we expect that any coupling of the plane wave mode from the input waveguide to the intermediate channel would be heavily suppressed due to mismatch in the characteristic acoustic impedance. In this case, the transmission would be dominated by the matching condition of

$$Z_1 = Z_2 \Rightarrow \frac{\sqrt{\rho_{eff\,1}\kappa_{eff\,1}}}{S_1} = \frac{\sqrt{\rho_{eff\,2}\kappa_{eff\,2}}}{S_2} \quad (3)$$

if $\kappa_{eff\,2} \to \infty$, assuming that $\rho_{eff\,1}\kappa_{eff\,1}$ represents a naturally-occurring fluid (and so the product would be positive and not very close to 0). Therefore, we may achieve both perfect impedance matching and phase uniformity in a hard-hard channel operated at a higher order mode, without interference in the phase pattern from the fundamental (*0,0*) mode.

Fig. 3 shows a length study for transmission amplitude and phase of the hard-hard waveguide. The same basic physics of the soft-hard configuration is verified, although the tunneling frequency is now $f = \frac{c_0}{a}$, corresponding to the (*2,0*) mode, rather than $f = \frac{c_0}{2a}$ of the (*1,0*) mode in the soft-hard configuration. We can see that the spatial phase pattern of Fig. 3b matches that of Fig. 2b in the center of the channel. In addition to this observation, we also observe that the first non-trivial cutoff frequency now occurs at the *(2,0)* mode of the intermediate channel, thus resulting in an "*effective soft boundary*", along the planes where the phase flips by π. This presents all of the typical properties associated with a soft-walled acoustic waveguide, although counter-intuitively, it is observed to occur within a waveguide having all hard boundary conditions. This concept

may be useful in designing waveguide structures which seek to avoid the fundamental (plane-wave) mode, but are confined to materials which are not substantially softer than the filling medium.

Next, we turn our attention to the performance of the proposed configuration for the acoustic CNZ channel when it is bent. It is expected that, due to the quasi-static nature of the pressure field near the cut-off frequency, the acoustic wave tunneling occurs regardless of the shape of the channel. Fig. 2c and Fig. 3c show the 2D phase profile of the pressure wave at the tunneling frequency for different bending cases, in which channels are bent *90°* and *180°*, for both the soft-hard and hard-hard configurations. It is clear that the phase is conserved through the channels and it is fully tunneled from the input to the output waveguide. This comparison also demonstrates the equivalency of operating a soft-hard waveguide in the $(m,n) = (1,0)$ mode and operating a hard-hard waveguide in the $(2,0)$ mode.

Finally, Fig. 4a shows a comparison of experimental results of CNZ supercoupling for an approximately hard-hard intermediate channel with numerical results for a similar geometry.

It can be seen from Fig. 4 that the measured data captures the basic physics of compressibility-near-zero supercoupling: impedance matching and near-zero phase delay in transmission, independent of the length of the intermediate channel. To aid in comparing numerical results to experiment, the model in Fig. 4 treated the boundaries of the coupling channel as elastic shells, which are capable of radiating sound into the surrounding air. This model also allowed for coupling of acoustic energy into vibrational modes of the walls, and for dissipation due to loss within the material (with $\tan\delta = 0.01$ for steel). This more realistic condition resulted in predicted transmission amplitudes with 8-13 dB of loss (depending upon the length), whereas the experimental results were more

consistent with 17 to 18 dB of loss. This agreement in transmission is good however, considering the uncertainties in material properties and variation of the intermediate channel geometry from an ideal rectangular prism. The data displayed lower-Q resonances as compared to the numerical results, which is expected from the imperfect parallel walls of the welder's trunk used in the experiment, which included some curvature and tilt at each boundary.

DISCUSSION

We have presented theoretical and experimental validation of a geometrically simple form of near-zero-index supercoupling in acoustics, which could be readily manufactured in any acoustics laboratory. While the experimental results did not show total transmission of acoustic energy, there is a good understanding of the underlying losses, as indicated by computational results, which considered radiation and dissipative loss in the intermediate channel. Further discrepancies between measurements and predictions can be explained by irregular geometry and uncertainty of material properties of the off-the-shelf toolbox used for the intermediate channel in the experiment. We estimate that the supercoupling transmission loss may be practically reduced below -1.9 dB if the intermediate channel were manufactured with a steel wall thickness of approximately 7.5 mm or higher (see Fig. 4a).

Compressibility-near-zero tunneling occurs when $S_2 \gg S_1$ (see Fig. 1), even in the case that all waveguides are filled with the same fluid. We can understand the supercoupling phenomenon as a dispersive impedance matching condition, which occurs when the coupling channel (with smaller characteristic impedance than the input waveguide) has an input impedance that appears nearly infinitely stiff. At this matching condition, the phase velocity approaches infinity, as long as S_2/S_1 is sufficiently large.

From this, we can achieve in principle, full amplitude transmission and total conservation of the phase, independent of the height and length of the coupling channel. Moreover, we show that such a waveguide, when driven near its cut-off frequency, exhibits compressibility-near-zero effective material properties. When this waveguide is constructed totally of hard boundaries and is operated at the (*2,0*) mode, it can be thought of as consisting of two effective soft boundaries. These effective soft boundaries consist of planar surfaces, along which the pressure field is equal to zero and the uniform phase of the tunneling mode flips by π.

We envision a wide-ranging applicability of the physics presented here, for use in acoustic sensing [31], for the tailoring of acoustic radiation patterns [32][33], for the production of Fourier transforms in the acoustic field through lensing [34], as well as for non-reciprocal and spatiotemporally-modulated acoustic devices.

METHODS

Analytical transmission line model for an acoustic supercoupling system

Suppose two identical waveguides, each with cross sectional area S_1, are filled with fluid #1 and have characteristic acoustic impedance Z_1. These waveguides are connected as an input and output to an intermediate rectangular acoustic channel (see Fig. 1), with length L and filled with fluid #2, having cross sectional area S_2 and characteristic acoustic impedance Z_2. Using transmission-line theory, the reflection coefficient for a plane wave in the input of this structure is written as

$$\Gamma = \frac{Z_1 - Z_{in}}{Z_1 + Z_{in}} \quad (4)$$

where Z_{in} is the impedance seen from the input waveguide when looking into the channel and it is calculated using

$$Z_{in} = Z_2 \frac{Z_1 + jZ_2 \tan(k_z L)}{Z_2 + jZ_1 \tan(k_z L)} \qquad (5)$$

where k_z is the wave number inside the intermediate channel. Plugging Eq. (5) in Eq. (4), the reflection coefficient reads:

$$\Gamma = \frac{(Z_2^2 - Z_1^2)\tan(k_z L)}{(Z_1^2 + Z_2^2)\tan(k_z L) + 2jZ_1 Z_2} \qquad (6)$$

To satisfy conservation of energy, a lossless system must obey $|T|^2 = 1 - |\Gamma|^2$. Thus, to achieve complete power transmission through the channel ($|T|^2 = 1$), the reflected power should become zero ($|\Gamma|^2 = 0$). The relation for reflection coefficient in Eq. (6) reveals that complete transmission is possible if $\tan(k_z L) = 0$ or $Z_2 = \pm Z_1$. The first condition corresponds to Fabry-Perot resonances and depends upon the length of the channel. However, the latter condition is achieved because of impedance matching. If we expand the impedance matching condition, $Z_2 = Z_1$, for the system of Fig. 1 and express it in terms of the effective material properties of each waveguide, we have Eq. (3), where ρ_{eff} and κ_{eff} are the effective mass density and bulk modulus respectively and denoted by subscripts of 1 for input/output waveguide and 2 for intermediate channel. When this condition is satisfied, we should expect full transmission through the system.

In addition to impedance matching, supercoupling phenomena display uniformity of phase through the coupling channel. In terms of the effective mass density and bulk modulus of the coupling waveguide, the uniformity of the phase can be related to wave number and interpreted as

$$k_z = \omega\sqrt{\frac{\rho_{eff\,2}}{\kappa_{eff\,2}}} \to 0 \qquad (7)$$

Then, in order to achieve supercoupling, where the wave is fully transmitted with uniform phase in the intermediate channel, both Eq. (3) and Eq. (7) must be satisfied.

Now, we can consider the cases in which supercoupling may be possible for the configuration of Fig. 1. For the sake of simplicity, suppose that the fluid in the input and output waveguides is fixed, and we can only alter the properties of the fluid in the intermediate channel (ρ_{eff2}, κ_{eff2}). In order to satisfy Eq. (7), one of the following criteria must be met:

- $\rho_{eff\,2} \to 0$: This case corresponds to the density-near-zero condition [23]. From Eq. (3), we can see that supercoupling requires $S_1 >> S_2$ (assuming that fluid #1 is a naturally occurring fluid, where $\rho_{eff\,1}\kappa_{eff\,1}$ is positive and not very close to 0).
- $\kappa_{eff\,2} \to \infty$: In this case, the stiffness of fluid #2 goes to infinity, which is equivalent to the compressibility tending toward zero ($\kappa_{eff\,2}^{-1} \equiv C_{eff\,2} \to 0$). Eq. (3) tells us that supercoupling now requires $S_1 << S_2$ (again assuming that fluid #1 has naturally occurring properties). We refer to this as the compressibility-near-zero (CNZ) condition and it is the focus of this paper.
- $\rho_{eff\,2} \to 0$ and $C_{eff\,2} \to 0$: When both fluid parameters simultaneously approach zero, this is the density-and-compressibility-near-zero (DCNZ) case [20][21][35]. Supercoupling may be achievable, however it is beyond the scope of this study.

Analytical description of cut-off in acoustic waveguides and acoustic compressibility-near-zero

For the wave propagating in an acoustic waveguide, the following relations can be written,

$$\begin{cases} \dfrac{\sqrt{\rho_{eff}\kappa_{eff}}}{S} = Z_z \\ \sqrt{\dfrac{\rho_{eff}}{\kappa_{eff}}} = \dfrac{k_z}{\omega} \end{cases} \qquad (8)$$

where Z_z and k_z are defined as acoustic impedance and wave vector in the z-direction and S is the cross-sectional area of the medium. Solving the system of Eq. (8) for (ρ_{eff}, κ_{eff}) results in

$$\begin{cases} \rho_{eff} = \dfrac{Z_z S k_z}{\omega} \\ \kappa_{eff} = \dfrac{Z_z S \omega}{k_z} \end{cases} \qquad (9)$$

To view Eq. (9) near the cut-off frequency, Z_z and k_z should be determined for the acoustic waveguide. Here, we can consider two different waveguide configurations with soft and hard walls. For example, consider a waveguide configured with two parallel soft boundaries at $x = \{0, a\}$ and two parallel hard boundaries at $y = \{0, b\}$. For this waveguide configuration, the spatial pressure distribution from the Helmholtz equation will be $p_{mn} = A_{mn}\sin(\frac{m\pi}{a}x)\cos(\frac{n\pi}{b}y)$ and it exhibits cut-off at discrete frequencies according to Eq. (2).

Due to the sinusoidal term in the pressure expression, $p = 0$ for $(m,n) = (0,0)$, thus preventing the propagation of the $(0,0)$ mode as the first mode. This results in a nonzero first cut-off frequency, $(m,n) = (1,0)$, which we denote as the first non-trivial cut-off frequency, that only depends upon the width of the channel (dimension a).

Now, if we use $p_{mn} = A_{mn}\sin(\frac{m\pi}{a}x)\cos(\frac{n\pi}{b}y)$ and the relation of conservation of momentum,

$$\nabla p + \mathrm{j}\omega\rho_0 u = 0 \qquad (10)$$

the particle velocity *u* is

$$u = -\frac{U_{mn}}{j\omega\rho_0}[k_x\cos(k_x x)\cos(k_y y)\hat{x} - k_y\sin(k_x x)\sin(k_y y)\hat{y} - jk_z\sin(k_x x)\cos(k_y y)\hat{z}]e^{-jk_z z} \quad (11)$$

And $Z_z = \frac{p}{Su_z}$ for the (*m*=1, *n*=0) mode, which will be calculated as in Eq. (1).

Then, by using Eq. (9) with Eq. (1), the effective material properties of the acoustic configuration with soft-hard boundaries near the (*1,0*) mode cutoff can be expressed in terms of the material properties of the filling fluid and dimensions of the channel by

$$\begin{cases} \rho_{eff\,2} = \rho_{0_2} \\ \kappa_{eff\,2} = \dfrac{\kappa_{0_2}}{1-(\dfrac{\pi c_0}{a\omega})^2} \end{cases} \qquad (12)$$

and it is observed that the value of the effective bulk modulus blows up with $f = \frac{c_0}{2a}$, and consequently compressibility tends to zero.

This CNZ condition results in supercoupling through the soft-hard channel. Note that it was shown in the previous section that for a configuration of Fig. 1, if the channel is designed with parameters such that $\kappa_{eff\,2} \to \infty\,(C_{eff\,2} \to 0)$ and $S_1 \ll S_2$, then supercoupling will occur at a particular frequency. It is also important to note that we have achieved a first-cutoff frequency that is greater than 0 Hz, because that will result in avoiding energy loss from the supercoupling mode to lower-order modes in the intermediate channel. However, despite the fact that soft-hard boundary conditions will

produce a waveguide with non-zero first cutoff frequency and consequently the effective compressibility-near-zero property, these boundaries can be difficult to realize in practical fluid media.

For a more realistic case, we can assume a waveguide configuration in which all boundaries are composed of a hard material. This is a typical description for many air-filled waveguides. In this case, the spatial pressure distribution is

$$p_{mn} = A_{mn} \cos(\frac{m\pi}{a} x) \cos(\frac{n\pi}{b} y) \qquad (13)$$

and the cut-off frequencies are also given by Eq. (2). Expression of pressure in Eq. (13) dictates that $p = A_{00}$ for $(m,n) = (0,0)$, thus the first cut-off frequency is zero and a plane wave mode can propagate for all frequencies. However, it can be seen that compressibility near zero (CNZ) occurs in a hard-hard waveguide that is operated near a higher cut-off frequency, with $(m,n) = (2,0)$, where $\kappa_{eff\,2} = \frac{\kappa_{0_2}}{1-(\frac{c_0}{af})^2}$ and the CNZ frequency is $f = \frac{c_0}{a}$.

Now, we must design the hard-hard supercoupling configuration in such a way that only the $(2,0)$ mode is excited while all previous modes $\{(0,0), (1,0), (0,1), \ldots\}$ are not. This can be accomplished by ensuring that the input signal is driven close to the center of the intermediate channel as well as enforcing the constraint that $S_1 \ll S_2$. These imposed geometrical restrictions prevent driving the odd modes, which must have a pressure null at the center of the input port. Furthermore, the even $(0,0)$ mode (plane wave mode) is also suppressed due to the large impedance mismatch between the input channel and the intermediate channel.

In this section, we showed that an acoustic channel with either soft-hard or hard-hard boundaries will have CNZ properties. This will occur while it is fed near the

geometric center of the channel and at a frequency near the appropriate cut-off frequency of a propagating mode, as long as the $S_1 \ll S_2$ condition is met. In other words, supercoupling can be achieved in either of these waveguide configurations. Moreover, Eq. (2) with *n=0* ensures that the cutoff frequency of such waveguides is independent of the waveguide's height (the dimension *b*) for corresponding supercoupling modes. Thus, we can freely design a channel with an arbitrary cutoff frequency, while ensuring the condition $S_1 \ll S_2$, by adjusting the parameter *b*.

Numerical Modeling

Finite element analysis was conducted by using Comsol Multiphysics. The Pressure Acoustics module was selected with the frequency domain solver. Air was chosen from the Comol built-in material list as the filling fluid of all structures. Finally, the input and output ports were set to Plane Wave Radiation conditions while the acoustic source was modeled as an Incident Pressure Field at the input port. In Fig. 1, the walls of the intermediate channel were modeled as either hard or soft boundary conditions. For the simulation of experimental parameters and consideration of vibrational coupling in the results of Fig. 4a, the supercoupoling system was first placed in an external rectangular domain filled with air. This domain enabled the modeling of leakage from the intermediate channel, and was bounded by Perfectly Matched Layers (PMLs) to realize non-reflecting boundaries. Materials were chosen from the built-in material library as Steel AISI 4340 for the intermediate channel walls and Aluminum for the input/output channel. The effects of visco-thermal acoustic boundary-layer loss were modeled by specifying the input/output waveguides as coupled to Narrow Region Acoustics. Then, walls of the intermediate channel were numerically modeled as thin elastic shells in the Comsol Acoustic-Shell Interaction Module. Finally, the Reflection and transmission

coefficient was calculated using the four-microphone measurement technique similar to [36] where, the value of complex k_z was derived from numerical simulations using complex sound speed.

Experimental Measurements

The experimental intermediate channel was built from an off-the-shelf steel welder's tool box with dimensions of a = 0.450 m, b = 0.382 m, L = 0.79 m, and wall thickness = 1.54 mm. The input and output waveguides were nearly-identical aluminum tubes with inside diameter = 12.6 mm, length of 92 cm, and thickness of 1.6 mm. The input waveguide was fed by a horn that was mounted transversely to the direction of propagation, and both input and output waveguides were terminated with anechoic foam to suppress standing waves in the tubes. Measurements were carried out with a procedure similar to [36] and following the standards of [37] and [38]. Due to the small dimensions of the input and output waveguides, a modest amount of acoustic boundary-layer loss was observed in the waveguides alone. This was corrected for by employing a complex value of k_z in the transfer-matrix equations, where $k_z = \beta + j\alpha$ and $\alpha \approx -0.13\,\mathrm{m}^{-1}$ according to [39].

CHAPTER 1 FIGURES

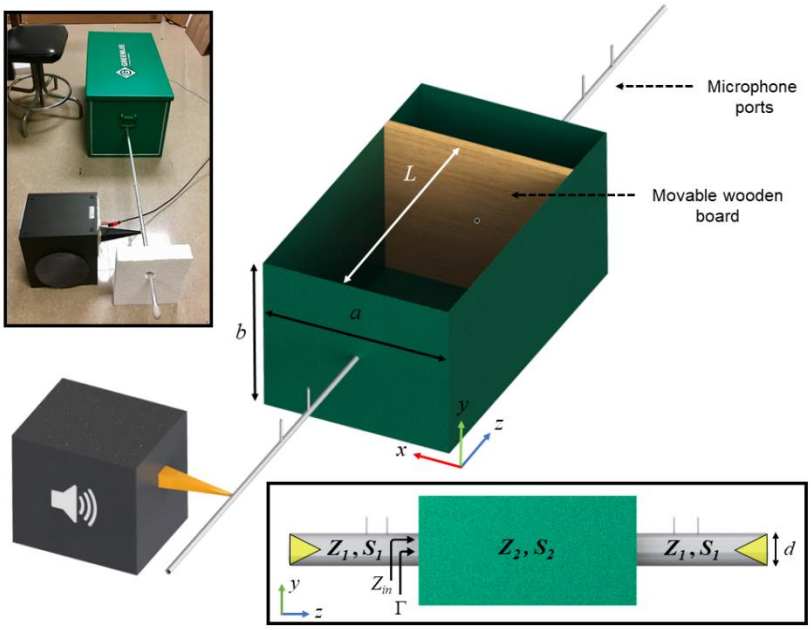

Fig. 1. Scale drawing of the experimental setup. Parts include an anechoic loudspeaker enclosure, an acoustic horn, input and output waveguides, the intermediate channel, a 1-inch thick Oak section (to adjust the effective channel length), and microphone ports. (*Inset bottom*)*:* Configuration of acoustic tunneling structure for the transmission line model. (*Inset top-left*)*:* Photograph of the experimental setup.

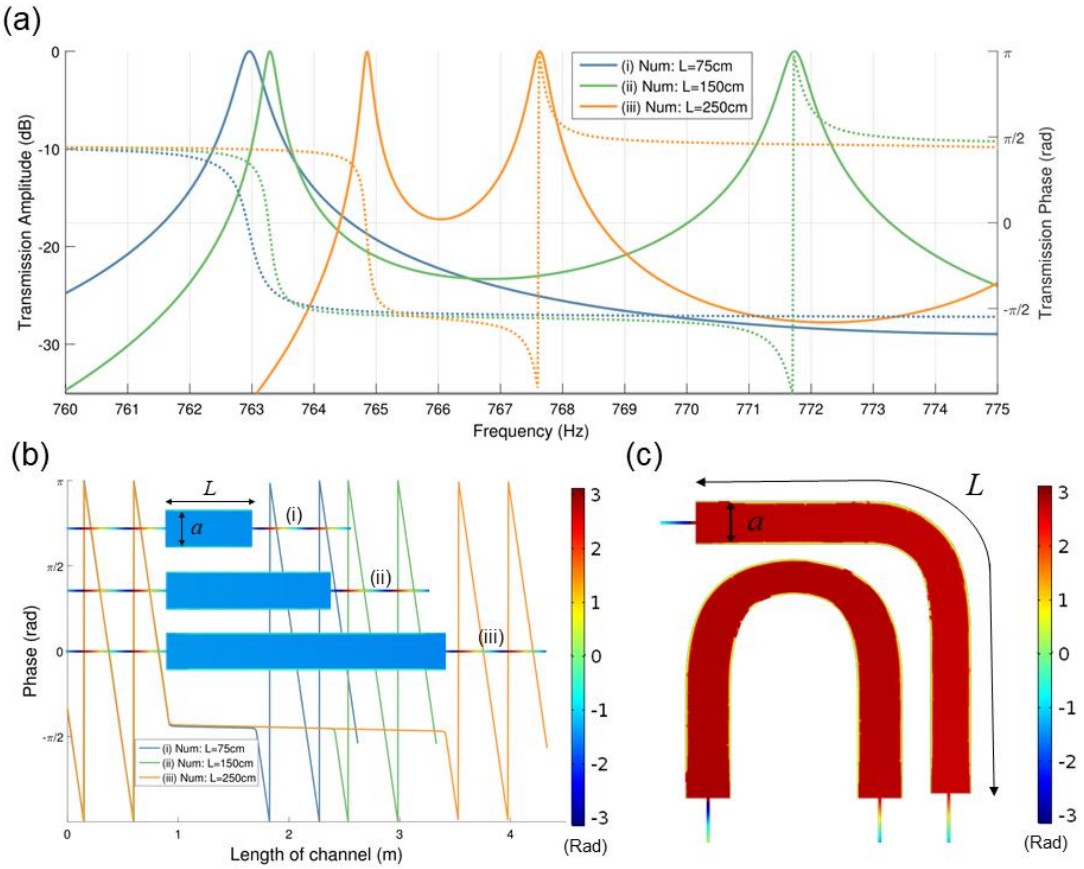

Fig. 2. Waveguides with two parallel soft and two parallel hard boundaries, operated near the first cut-off frequency. **a.** Numerical results for transmission phase and amplitude. The design parameters were similar to the experimental setup, with only the length being modified. These show nearly unitary transmission amplitude independent of the length of the coupling channel (a = 0.225 m, b = 0.382 m, and d = 12.6 mm). **b.** Phase distribution through the CNZ channel near the first cut off frequency for configurations of different lengths. $f_{tunneling}$ (i) = 763.0 Hz, $f_{tunneling}$ (ii) = 763.3 Hz, $f_{tunneling}$ (iii) = 764.9 Hz. **c.** Spatial variation of phase at the CNZ tunneling frequency for waveguides with 90° and 180° bends. We observe uniformity of the phase despite bending of the channel. Here, a = 0.225 m, b = 0.382 m. $f_{tunneling\_90}$ (i) = 756.92 Hz, $f_{tunneling\_180}$ (ii) = 756.76 Hz.

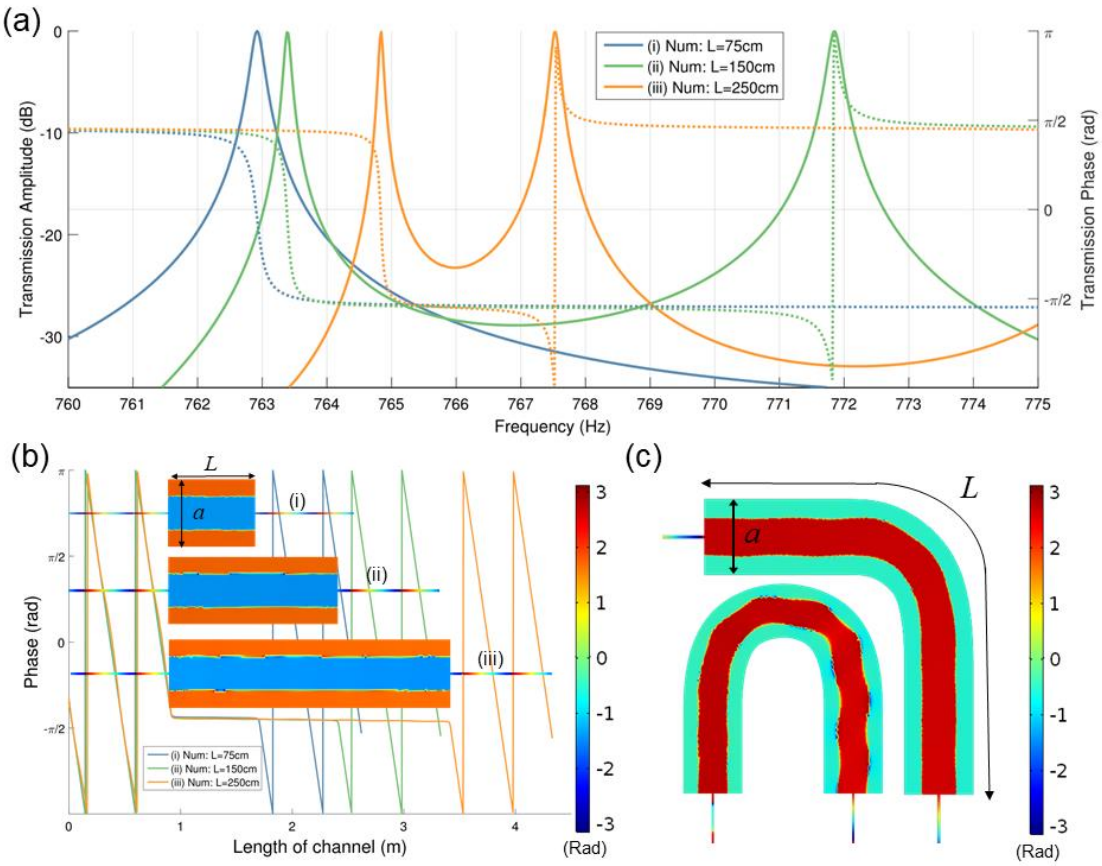

Fig. 3. Waveguides with parallel hard boundary conditions, operated near the higher-order *(2,0)* mode of the intermediate channel. We can see the higher-order mode matches the phase pattern of the soft-hard (*1,0*) mode (from *Fig. 2*) in the center of the channel. This presents an "*effective soft boundary*" along the planes where the phase flips by π. This flip results from a change in sign of the pressure, which is a purely real-valued standing wave. **a.** Numerical results for transmission phase and amplitude. The design parameters were similar to the experimental setup, with only the length being modified (a = 0.450 m, b = 0.382 m, and d = 12.6 mm). **b.** Phase distribution through the CNZ channel near the (*2,0*) cut-off frequency for hard-hard configurations of different lengths. For bottom figure: $f_{tunneling}$ (i) = 762.9 Hz, $f_{tunneling}$ (ii) =

763.4 Hz, $f_{tunneling}$ (iii) = 764.8 Hz. **c.** Spatial variation of phase at the CNZ tunneling frequency under 90° and 180° bends. Here, a = 0.450 m, b = 0.382 m, $f_{tunneling}$ (i) = 764.2 Hz, $f_{tunneling}$ (ii) = 758.97 Hz.

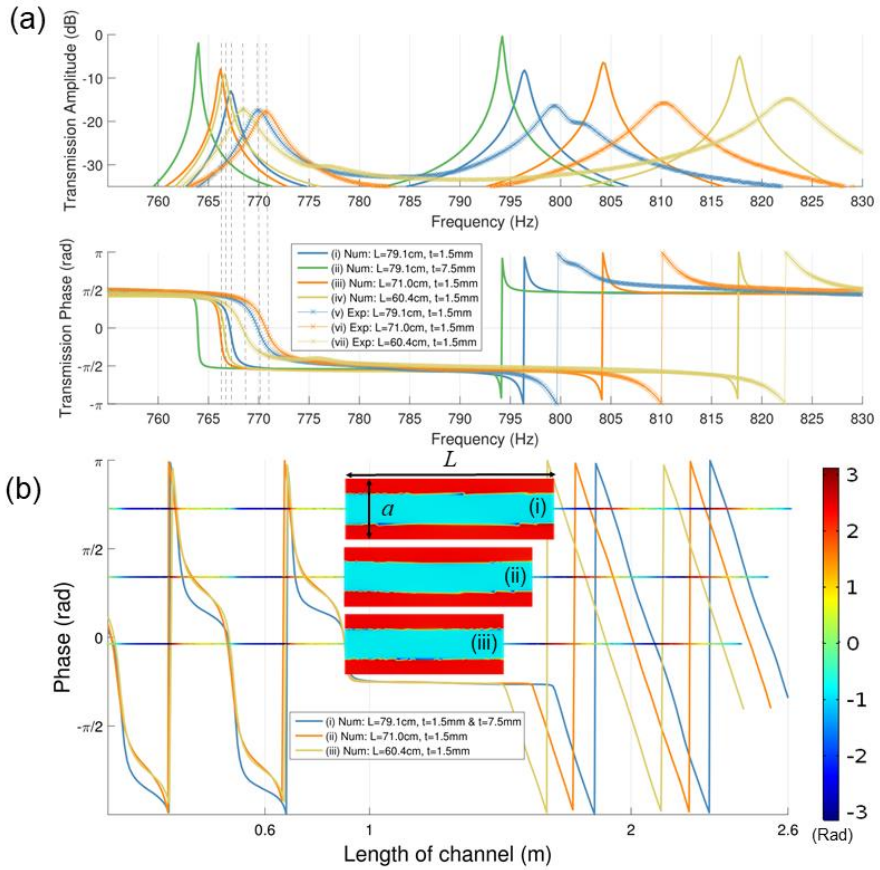

Fig. 4. Experimental measurements and numerical results for the hard-walled supercoupling channel. a. Numerical and experimental comparison for the transmission phase and amplitude. Radiation and material loss from the intermediate channel were modeled using elastic shell boundary conditions with a loss tangent of 0.01. Note that curve (ii), in red, shows the transmission amplitude at the tunneling frequency (~765 Hz) is much higher than the others, due to the use of thicker walls for the intermediate channel. The experimental parameters were a = 0.450 m, b = 0.382 m, and d = 12.6 mm. **b.** Spatial phase distribution through the CNZ channel at the tunneling frequency for configurations with different lengths and $f_{tunneling}$ (i) = 767.1 Hz, $f_{tunneling}$ (ii) = 766.2 Hz, $f_{tunneling}$ (iii) = 766.6 Hz.

Chapter 2: A Uniform-Phase Acoustic Power Divider with Compressibility-Near-Zero Effective Material Properties[2]

INTRODUCTION

Recently, near-zero-index metamaterials have received much attention due to their extraordinary capabilities in wave manipulation, which stems from their temporally and specially decoupled nature [1]. Although the majority of this research has been in the electromagnetic realm, regarding media with near-zero dielectric permittivity, near-zero magnetic permeability or double-near-zero materials [11][12], recent attention has also been given to analogous phenomena in the fields of plasmonics [15], photonics [17][18], and acoustics [23]. Several novel concepts such as cloaking [24] and supercoupling [23] have been developed in near-zero-index media both for electromagnetic and acoustic fields. Furthermore, numerous contemporary applications have been developed and experimentally validated, such as increasing the directivity of a radiating body [26], realizing a monopolar electromagnetic antenna [40], an acoustic leaky-wave antenna with broadside radiation [20],[21], and an electromagnetic N-port series power divider [41]-[44].

Among the proposed applications, the latter is of utmost importance in microwave engineering because power dividers are used for dividing signals between amplifier chains, for feeding networks in array antennas, and for the distribution of microwave signals to subsystems [41]. Power dividers, as an essential part of the feeding network in array antennas, are classified in three different categories: parallel, series, and hybrid (parallel-series), each having their own advantages, disadvantages, and specific

[2] Portions of this chapter are planned for publication as a part of a group effort. This work was completed with Hussein Esfahlani and myself as first co-authors, followed by and Andrea Alù as an additional author. Hussein Esfahlani initiated the research. Hussein and I spent equal effort in developing the analytical theory and on the numerical simulations. Andrea Alù supervised the research.

applications [45]. For example, the design of antenna arrays with equal amplitude/phase excitation with a main beam at broadside is popular in telecommunications. The feeding network for such array antennas can be parallel, series or hybrid. However, series power dividers are preferred when we deal with a limited physical space, because parallel-divider-based networks are usually bulky due to the three-port shape of the parallel power divider [41]. In a series feed network, the meander line technique is leveraged to ensure that each antenna element is fed with an equal amplitude and equal phase signal. Hence, there is a cumbersome requirement that the signal be sampled from the meander feed line at locations which are integer multiples of the guided wavelength [42]. Therefore, although series power dividers have many advantages, they also have various drawbacks such as additional design complexity, restrictions imposed upon the placement of antenna elements in the array, and they must be custom tailored according to the number of elements [43]. However, it can be shown that by leveraging the infinite-wavelength phenomenon based on near-zero index media, a new type of series power divider can be designed where the aforementioned drawbacks can be overcome and significant size reductions compared to meander line series power dividers may be achieved.

In this paper, we propose the acoustic counterpart of the infinite-wavelength electromagnetic series power divider by following advances of electromagnetic near-zero index media and by leveraging the infinite wavelength of an acoustic wave in a compressibility-near-zero (CNZ) medium. To this end, we extend theoretical and experimental findings from Chapter 1 in realizing a CNZ supercoupling medium to design an N-port acoustic series power divider. We provide analytical and numerical formulations to prove and support the concepts. Then, the proposed N-port series power divider is demonstrated to have novel functionality, such as operation with an arbitrary number of ports for equal amplitude and equal phase power division. Furthermore, the

divider may be configured to divide the signal with a phase flip of π radians, alongside with equi-phase output ports. Additionally, further features of the proposed concept are numerically investigated, such as tuning the amount of power at each output port and scaling the length and height of the coupling channel while maintaining the CNZ tunneling condition. Finally, an analysis of practical trade-offs due to losses are made in a discussion of the scalability of the device.

THEORY

In a near-zero-index material, it can be shown that the governing wave equations will be temporally and spatially decoupled [11]. For acoustic phenomena, this results in a pressure field that is uniform throughout the medium, therefore if the signal is sampled from such a medium the output signals are expected to have equal phase. To demonstrate this theoretically, let us consider the following scenario where several input/output channels are connected to an intermediate medium with near-zero-index properties, as shown in Fig. 5.

Equi-Phase Power Division

In this case, we assume that the effective compressibility, C_{eff}, is zero and thus $\lambda = \frac{1}{f}\sqrt{\frac{1}{C_{eff}\,\rho_{eff}}} \to \infty$. Channel #1 (with characteristic acoustic impedance Z_1) is the input and the other channels (with characteristic acoustic impedance Z_j) are dedicated for the output. Z_j is defined as $Z_j = \frac{\rho_j\, c_j}{S_j}$, where $j \in [2, N]$ is the index of each output channel and ρ_j , c_j and S_j are respectively the mass density, sound velocity, and cross sectional area of the channel j.

As the pressure in the intermediate medium is constant, the pressure boundary condition is

$$p_{i1}^{+} + p_{i1}^{-} = p_{t2} = p_{t3} = ... = p_{tN} \qquad (14)$$

Which can be simplified and written as,

$$1 + R_1 = T_2 = ... = T_N \qquad (15)$$

Where R_1 and T_x $x \in [2, N]$ are the reflection and transmission coefficient of the input and output channels respectively.

By applying the particle velocity boundary condition, the volume velocity q reads:

$$q_{i1}^{+} + q_{i1}^{-} = q_{t2} + q_{t3} + ... + q_{tN} \qquad (16)$$

And, assuming plane wave propagation in the input/output waveguides, it can be expressed in terms of pressure as,

$$\frac{p_{i1}^{+}}{Z_1} - \frac{p_{i1}^{-}}{Z_1} = \frac{p_{t2}}{Z_2} + \frac{p_{t3}}{Z_3} + ... + \frac{p_{tN}}{Z_N} \qquad (17)$$

This relation can be simplified as,

$$1 - R_1 = Z_1 \left(\frac{T_2}{Z_2} + \frac{T_3}{Z_3} + ... + \frac{T_N}{Z_N} \right) \qquad (18)$$

By substituting Eq. (15) into Eq. (18), the reflection and transmission coefficient of the input and output channels are derived and expressed respectively by,

$$R_1 = \frac{Z_1^{-1} - \sum_{j=2}^{N} Z_j^{-1}}{\sum_{j=1}^{N} Z_j^{-1}} \qquad (19)$$

$$T_x = 1 + R_1 = \frac{2Z_1^{-1}}{\sum_{j=1}^{N} Z_j^{-1}},\ x \in [2, N] \quad (20)$$

Where the power transmission and reflection coefficients are defined by $T_{\Pi x} = \frac{Z_1}{Z_x}|T_x|^2$ and $R_{\Pi 1} = |R_1|^2$, respectively [46]. It is clear that for a two-port structure, where Z_1=Z_2, that no signal is reflected back into the input while all of the energy is tunneled through the intermediate medium into the output. Now let us consider the condition where the characteristic acoustic impedance of the input/output channels are all the same ($Z_1 = Z_2 = ... = Z_N$), which results in the following expressions for the reflection and transmission coefficients for amplitude and power:

$$R_1 = \frac{2}{N} - 1,\ R_{\Pi 1} = \frac{4}{N^2} - \frac{4}{N} + 1 \quad (21)$$

$$T_x = \frac{2}{N},\ T_{\Pi x} = \frac{4}{N^2} \quad (22)$$

Where N is the total number of ports in the power divider ($N \geq 2$). The relations of Eq. (21) and (22) reveal that:

1. If the number of the output channels is increased, the amount of the reflected power will rise.
2. The amount of the transmitted power is inversely proportional to the square of the number of the output ports.
3. If the number of the output ports is limited to 1 or (N=2) then the tunneling condition arises with T_2=1, R_1=0.

Equi-Phase Zero-Reflection Power Division

Moreover, an analysis of Eq. (19) and Eq. (20) reveals that, when the number of the output ports is greater than one, the reflected power can be suppressed if:

$$Z_1^{-1} = \sum_{j=2}^{N} Z_j^{-1} \qquad (23)$$

Hence, as far as the aforementioned relation is satisfied, the input power can be divided between the output ports with equal phase and without reflection, irrespective of the distribution of the acoustic characteristic impedance of the output ports, while only putting a constraint on their sum.

Equi-Phase and Equi-Amplitude Zero-Reflection Power Division

Furthermore, the output power can be evenly divided among the ports if the characteristic impedance of each output port (Z_j) is equal. To theoretically demonstrate this, Eq. (23) can be further expanded using the material properties as well as geometrical dimensions of the channel, as

$$\frac{S_1}{\rho_1 c_1} = \frac{S_2}{\rho_2 c_2} + \frac{S_3}{\rho_3 c_3} + \ldots + \frac{S_N}{\rho_N c_N} \qquad (24)$$

If the material inside the input and output channels are chosen to be the same, or in other words the specific acoustic impedances of the channels were equal, then the aforementioned relation is simplified in the following form

$$S_1 = S_2 + S_3 + \ldots + S_N \qquad (25)$$

This relation reveals a matching condition for the CNZ power divider similar to the configuration of Fig. 7, which will completely suppress the reflected power from the input. For this to happen, the sum of the cross-sectional areas of the output channels should be equal to the cross-sectional area of the input channel (when the materials in the input and output channels are identical).

NUMERICAL SIMULATIONS

Now let us turn to the realization of such a CNZ power divider. Previously in Chapter 1, it was shown that it is possible to achieve an effective compressibility near-zero medium by exciting a hard-walled acoustic waveguide with a rectangular cross section at exactly the cutoff frequency of its (2,0) mode. Moreover, it was shown that in order to achieve good impedance matching, the ratio of the cross-sectional areas of the input/output waveguides to the intermediate tunneling channel should be very small. This constraint can be expressed as

$$S_j << S_{ch} \quad \forall j \in [1, N] \quad (26)$$

where S_{ch} is the cross-sectional area of the intermediate channel that will exhibit CNZ properties and N is the total number of waveguides connected to the intermediate channel. Following these principles, a finite element model was constructed in Comsol Multiphysics, employing the Pressure Acoustics module and frequency domain solver. Air was chosen from the Comol built-in material list as the filling fluid of all structures. Finally, the input and output ports were set to Plane Wave Radiation conditions while the acoustic source was modeled as an Incident Pressure Field at the input port. Sound hard boundary conditions were used to model the walls of the input/output waveguides as well as the intermediate channel. Parameters for figures 2 through 5 were chosen such that the CNZ channel had dimensions of a = 0.450 m, b = 0.382 m, and L = 0.79 m, similar to the experimental setup of Fig. 1. Results are shown in Fig. 6 and Fig. 7, where the described system was operated with three output ports, following the constraints of Eq. (22) and Eq. (25) in each figure respectively.

Considering the Lossless Case

Fig. 6 shows the power reflection and transmission coefficients for a 4-port CNZ power divider. In this configuration, all input/output waveguides have the same cross-sectional areas and are filled with air. The output ports are placed at the top-center of the channel, where the phase of the CNZ resonance is uniform and equal to the input phase. At the CNZ frequency (763 Hz) this results in equal power division with uniform phase to all of the output ports (Fig. 6a); however, there is a reflection of the incident energy, such that 25 percent of the power is reflected back (Fig. 6b), in agreement with Eq. (21) and Eq. (22).

In order to suppress the reflected power and couple all of the input energy to the output of the system, a second configuration was constructed following the conditions of Eq. (25), and this is shown in Fig. 7. In this case, all of the dimensions and materials are kept constant with respect to Fig. 6, except for the cross-sectional areas of the output waveguides, which are each smaller by a factor of three, therefore the sum of the cross sections of the outputs is equal to the cross section of the input channel. By examining this figure, we can verify that there is impedance matching at the CNZ frequency and therefore full power transmission of the input signal with zero reflection at the input, while the power is split evenly among the three output channels with equal phase, as expected from Eq. (23).

The CNZ mode profile represents a standing wave in the x-direction of Fig. 6, where the frequency of the mode depends upon the width of the intermediate channel, a, and is independent of the length, L, and the height, b (given that Eq. (26) is also satisfied). This result is in contrast with that of the higher-order resonance (the second peak in Fig. 6 and Fig. 7) which depends upon the length of the channel, analogous to the Fabry-Perot resonances observed in electromagnetics [15]. The phase distribution of this

higher-order mode is not uniform along the channel length (see Fig. 7d), and therefore does not provide power equally to all ports.

Furthermore, it should be noted that the matching condition of Eq. (25) does not require all output ports to have the same cross-sectional area. When this condition is met with unequal cross sections, the power distribution can be tuned at each of the output ports, as shown in Fig. 8. In this case, the geometrical and material parameters were kept constant with respect to Fig. 7, except that the cross-sectional areas of the outputs were set to $S_2=S_1/6$, $S_3 = S_1/3$, and $S_4 = S_1/2$, such that $S_1=S_2+S_3+S_4$ and Eq. (25) is satisfied. This resulted in an impedance-matched power divider, where no reflection is seen at the input, but where the amount of power distributed to each output is equally proportional to S_j/S_1, such that $P_2=P_{in}/6$, $P_3=P_{in}/3$, and $P_4=P_{in}/2$. The tuning of output power can prove useful in some applications, such as making interferometric measurements of a lossy sample, where there are two output channels: one being an empty reference channel (without material loss), and a second being filled with some lossy material [47]. By increasing the output power to the sample's channel, the system can be designed to compensate for the material loss and compare the phase of two signals having equal power.

Another unique feature of the proposed configuration is that the phase of the (2,0) mode within the channel is flipped by 180 degrees near the boundaries on the sides of the channel, (see Fig. 9). In this case, all geometrical and material parameters are the same as Fig. 7, except for the locations of the output waveguides, which were placed with two outputs along the side and with one output along the end-face. It can be seen that impedance matching, and thus full power transmission, is still achieved (Fig. 9a), even in the case that output ports are installed transverse to one another. More importantly, the signal that is coupled to the side channels (#2 and #3) is the phase inverted (180-degree

phase-flipped) version of the output signal along the end face (channel #4). Fig. 9 also highlights the capability of inverting the phase of some output channels, while preserving the input phase of one (or more) channel(s).

As previously discussed, CNZ-based series power dividers are also expected to have invariant performance with changes in the length and height of the coupling channel. To demonstrate this, a more general case of the power divider is shown in Fig. 10, where both the length and height are changed with respect to the previous figures; additionally, the number of output ports is increased to five, and output ports are placed along all faces of the intermediate channel (except for the input face). In this case, the cross-sectional area of the input port is the same as in figures 6 through 9, however the cross-sections of all output ports are now equal to $S_{in}/5$, in order to satisfy Eq. (25). We see that impedance matching still occurs at the CNZ frequency (Fig. 10b), while the phase of the output signal will be either 0 degrees or 180 degrees, depending upon the placement of each port (see Fig. 10a).

Modeling Lossess Due to a Finite Boundary Thickness and Scaling the Dimensions

Finally, a study was carried out to assess the scalability of the uniform-phase acoustic power divider. In particular, downscaling the device is emphasized because it could enable a less bulky package that would be easier to fit in a finite-sized acoustic system. Additionally, shrinking the dimensions might permit significantly lower radiation losses than those observed experimentally in Fig. 4. This can occur because a smaller channel would require a higher frequency for the excitation of the CNZ mode, which corresponds to a shorter wavelength in the transverse direction within the channel (where λ is not infinite).

To further understand this concept, we can approximate the radiation loss in the intermediate channel due to finite thickness (i.e. l=1.5mm) of an approximately sound-hard wall (i.e. steel) by characterizing the channel as a resonant cavity having a total quality factor which depends upon both a loaded and unloaded quality factor, $\frac{1}{Q} = \frac{1}{Q_{loaded}} + \frac{1}{Q_{unloaded}}$. In this case, the loaded quality factor represents the case when the channel is attached to the output waveguides (which act as the load), but has perfect hard boundaries (there is not any radiation). Then, it follows that the unloaded quality factor represents the case when the output ports are blocked (in other words, the load is removed) and the boundaries allow for radiation. The former case has already been modeled in numerical results from figures 2-6, where the channel has $Q_{loaded} \equiv \frac{f_r}{\Delta f} \approx 7500$. This value can change depending upon the length, height, and number of output ports, however $Q_{loaded} \approx 7500$ will be used as an estimate in this example.

To find an expression for $Q_{unloaded} \equiv 2\pi \frac{W_{stored}}{W_{rad}}$ (where W_{stored} is the steady-state energy stored in the cavity in one period and W_{rad} is the energy radiated in one period), we approximate the power lost from each transient reflection by using the power transmission coefficient through an acoustic slab with finite thickness, l, at normal incidence [39]:

$$T = \frac{4}{4\cos^2(k_{steel}l) + (\frac{Z_{steel}}{Z_{air}} + \frac{Z_{air}}{Z_{steel}})^2 \sin^2(k_{steel}l)} \qquad (27)$$

The normal incidence assumption is justified because the monomodal (2,0) mode in the cavity resonates in a direction that is normal to two of the boundaries (from which we expect nearly all of the radiation to occur). Then a standing wave in the resonator with

power $\frac{|a|^2}{2Z_{air}}$ will lose an amount of power $T\frac{|a|^2}{2Z_{air}}$ at the first transient reflection and it will lose $T(1-T)\frac{|a|^2}{2Z_{air}}$ at the second transient reflection. If we assume that $(1-T)\approx 1$ (for example, for the intermediate channel of figures 2-6, $T \approx 2.25\cdot 10^{-4}$) then a power of $T\frac{|a|^2}{2Z_{air}}$ is radiated after each reflection with a total of two reflections per period. This results in a radiated power per cycle of $P_{rad} = \frac{T|a|^2}{Z_{air}}$. In terms of energy we have $W_{rad} = \frac{2\pi}{\omega}P_{rad}$. The stored energy in the resonator in each cycle is twice the energy density of a single reflection multiplied by the length of the cavity, $W_{stored} = 2\frac{P_{stored}}{c}L = 2\frac{\frac{|a|^2}{2Z_{air}}}{c}L = \frac{|a|^2 L}{Z_{air}c}$. Finally, this results in

$$Q_{rad} \equiv Q_{unloaded} \equiv 2\pi\frac{W_{stored}}{W_{rad}} = \frac{\omega L}{Tc} = \frac{2\pi}{T} \qquad (28)$$

(where again, T is the power transmission coefficient from Eq. (27) rather than the period).

Now that we have Q_{loaded} and $Q_{unloaded}$, we can use coupled mode theory to make a first-order approximation for the amount of power radiated from the cavity [48].

$$\frac{da}{dt} = (i\omega_0 - \gamma)a + \kappa s_{inc} \qquad (29)$$

Here, a is the mode amplitude in the cavity, ω_0 is the cavity's resonance frequency, $\gamma = \gamma_{loaded} + \gamma_{unloaded} = \frac{\omega_0}{2Q}$ is the total decay rate, κ is the coupling coefficient, and s_{inc} is the input waveform. Assuming that we are operating the cavity at the CNZ frequency, then $\omega = \omega_0$ and $s_{inc} = e^{i\omega_0 t}$. From this, we find

$$a = \frac{\kappa}{\gamma} \quad (30)$$

And, given that $\kappa^2 = 2\gamma_{loaded}$ [48], then

$$P_{rad} = 2\gamma_{rad} \mid a \mid^2 = 2\gamma_{rad} \frac{\mid \kappa \mid^2}{\gamma^2} = \frac{4\gamma_{rad}\gamma_{loaded}}{(\gamma_{rad} + \gamma_{loaded})^2} = \frac{4Q_{rad}Q_{loaded}}{(Q_{rad} + Q_{loaded})^2} \quad (31)$$

where in the final expression we used $\gamma_{rad} = \frac{\omega_0}{2Q_{rad}}$ and $\gamma_{loaded} = \frac{\omega_0}{2Q_{loaded}}$. This expression can now be used to approximate the power radiated from the cavity with an acoustic boundary of finite thickness and finite impedance. For illustrative purposes, we will consider two cases:

1. $f_0 = 763$ Hz, corresponding to the examples presented in figures 2-6, having an intermediate channel with a width of 45 cm, but now with a steel wall of finite thickness 1.5 mm (rather than an ideal hard boundary).
2. $f_0 = 10,000$ Hz, corresponding to a power divider that has all dimensions downscaled proportionally to case 1, resulting in a significantly smaller channel width of 3.4 cm, however having the same steel wall thickness of 1.5 mm.

From Eq. (27), the first case results in $T \approx 2.25 \cdot 10^{-4}$ and $Q_{rad} = 2.80 \cdot 10^4$. Combining these values with the numerical results of $Q_{loaded} \approx 7500$, we have from Eq. (31) that $P_{rad} \approx 0.67$ (and we see that there is very high radiation loss at this size scale). In the second case, it is assumed that the scalability property of the lossless Helmholtz

equation ensures that the loaded quality factor of the smaller power divider in case 2 will remain the same as in case 1 (this fact was also verified numerically). Then, given the new value of k_{steel} in Eq. (27), we observe that $T \approx 1.31 \cdot 10^{-6}$ and $Q_{rad} = 4.80 \cdot 10^{6}$, resulting in a much lower $P_{rad} \approx 0.01$ from Eq. (31). The significantly lower value for T in the second case (with a smaller intermediate channel) is expected intuitively, due to the walls being much thicker with respect to the wavelength, changing from $\lambda / l \approx 300$ in the first case to $\lambda / l \approx 23$ in the second case. These results highlight the concept that downscaling the size of the intermediate channel can significantly reduce radiation losses (assuming that the wall thickness will practically increase with respect to λ as we increase the CNZ operating frequency).

Considering the Influence of the Visco-Thermal Acoustic Boundary Layer

Despite the theoretical benefits of downscaling the size of the system, one major barrier that exists is acoustic boundary layer loss, which results from the viscosity of the medium in contact with the boundary as well as the thermal conductivity of the waveguide perimeter. Due to this mechanism, it is expected that the losses within the input and output waveguides will increase as their sizes are decreased [39] [49].

In order to counter-act the boundary layer loss due to the down scaling of the size of the power divider, the input/output waveguide sizes were increased relative to the intermediate channel and a parametric study was performed to test the restrictions of Eq. (26) on the performance of the power divider. It was observed that, as the size of the input waveguide is increased, both the phase uniformity and the impedance matching of the CNZ mode begin to degrade. Fig. 11a and Fig. 11b show an example of a case study where the radius of the largest waveguide is increased to $a/8$ (where a is the width of the intermediate channel) and the radii of all output waveguides are equal to $a/(8\sqrt{5})$ in

order to satisfy Eq. (25). The increased size of the waveguide radius with respect to the width of the intermediate channel results in degradation of impedance matching, increased reflected power, and uneven power division (with respect to the previous configurations of figures 3 through 6). Here, the power reflection coefficient reaches a minimum value of 0.03 and can be compared to previous configurations, which fully satisfied Eq. (26), and showed a minimum reflected power of 0. Additionally, as dictated by Eq. (25), it is expected to have power divided equally among the output ports with power transmission coefficient of 0.2 per output channel. However, in this case the power is distributed differently at each port, where the minimum power transmission coefficient is 0.181 at port 2 and port 4, and the maximum power transmission coefficient is 0.204 at ports 3, 5, and 6. This corresponds to a maximum variation in the power transmission coefficient of 11.5% with respect to the expected value of 0.2. Finally, note that the phase of the outputs along the central channel are no longer close to zero, but have each shifted to approximately $\pi / 4$ rad.

The amount of boundary layer loss at various size scales can also be quantified. By considering the scale invariance of the Helmholtz equation in the waveguides and intermediate channel (without boundary layer loss), all dimensions of the power divider can be decreased proportionally while the frequency is increased, such that the size of each dimension with respect to λ stays constant. This theoretically yields a device with identical performance, except for the considerations of visco-thermal loss, which depends upon both the frequency and the dimension of each waveguide, and the radiation loss that depends upon the thickness of the waveguide and intermediate channel. Previously we showed that radiation loss can be controlled independently by setting the thickness of the walls of the intermediate channel. Now we can predict the boundary layer loss upon

scaling the power divider by considering the smallest waveguide in the system, which is the limiting factor that produces the greatest amount of loss.

We can express the particle velocity in that waveguide as $u = u_0 e^{-\alpha z} e^{j(\omega t - \beta z)}$, where for a gas medium,

$$\alpha = -\mathrm{Im}\left\{ \frac{\omega / c_0}{\sqrt{1 - \frac{2}{a}\left(1 + \frac{\gamma - 1}{\sqrt{\mathrm{Pr}}}\right)\sqrt{\frac{\nu}{j\omega}}}} \right\} \qquad (32)$$

with *a* being the radius of the cylindrical waveguide, γ the ratio of specific heats, *Pr* is the Prandtl number, and υ is the kinematic viscosity [39]. By assuming standard atmospheric conditions in air, the implications of Eq. (32) are considered in Fig. 11d. In this figure, we can see the maximum waveguide radius (black curve), which represents the degradation level examined in Fig. 11a and Fig. 11b. We can consider the radius that corresponds to this degradation level as our maximum acceptable tolerance. Then it is possible to construct an acoustic power divider within an acceptable phase and amplitude variation range by selecting any point in Fig. 11d below the black curve. Moving to the right on the x-axis of the plot (changing the frequency) will result in downscaling the dimension of the coupling channel (where $a = \lambda$), while moving down on the y-axis (reducing the size of the smallest waveguide in the system) will improve the phase uniformity. It can be seen that improved phase uniformity comes at the cost of increased boundary-layer loss. Therefore, careful consideration of the signal requirements for each application should be made before choosing the size of the channel, the size of the input/output waveguides, and the frequency of a given device. Finally, it should be noted that phase uniformity can also be improved by increasing the height of the channel (*b*),

which should have a negligible impact on the operating frequency (CNZ frequency) of the power divider, as shown in Chapter 1.

CONCLUSION

By leveraging the fundamental concepts of acoustic supercoupling that were developed in Chapter 1, it was shown that a novel acoustic power divider can be practically realized. This power divider has unique features, such as the capability of transmitting power with uniform phase to an arbitrary number of output ports, independent of the placement of the ports along the central region of the channel. Additionally, it was shown that this power divider can maintain its functionality, independent of changes in the length and height of the coupling channel, given that there is a large difference between the cross-sectional areas of the input/output waveguides and the cross-sectional area of the coupling channel. Furthermore, by designing the acoustic channel to support a compressibility-near-zero (CNZ) condition with hard boundary conditions in a higher-order mode, it is possible to invert the phase (by π radians) at an arbitrary number of output ports without compromising impedance matching in the device. This approach also overcomes limitations of traditional meander-line-based series power dividers, which require the output ports to be constrained to specific locations along the length of the component.

It was also shown that, in the absence of material loss and radiation loss, that the input and output ports can be designed to fully couple the incident power to an arbitrary number of output channels. Moreover, an additional capability of the uniform phase power divider was discussed, in which the amount of power to each port could be tuned while maintaining impedance matching in the system. Finally, by evaluating the trade-offs between visco-thermal loss, radiation loss, phase uniformity, and power splitting, a

practical avenue towards more compact and lower-loss CNZ supercoupling was proposed. This opens possibilities for new centimeter-scale acoustic supercoupling devices with potential applications in wave shaping, sensing, filtering, and interferometry.

Chapter 2 Figures

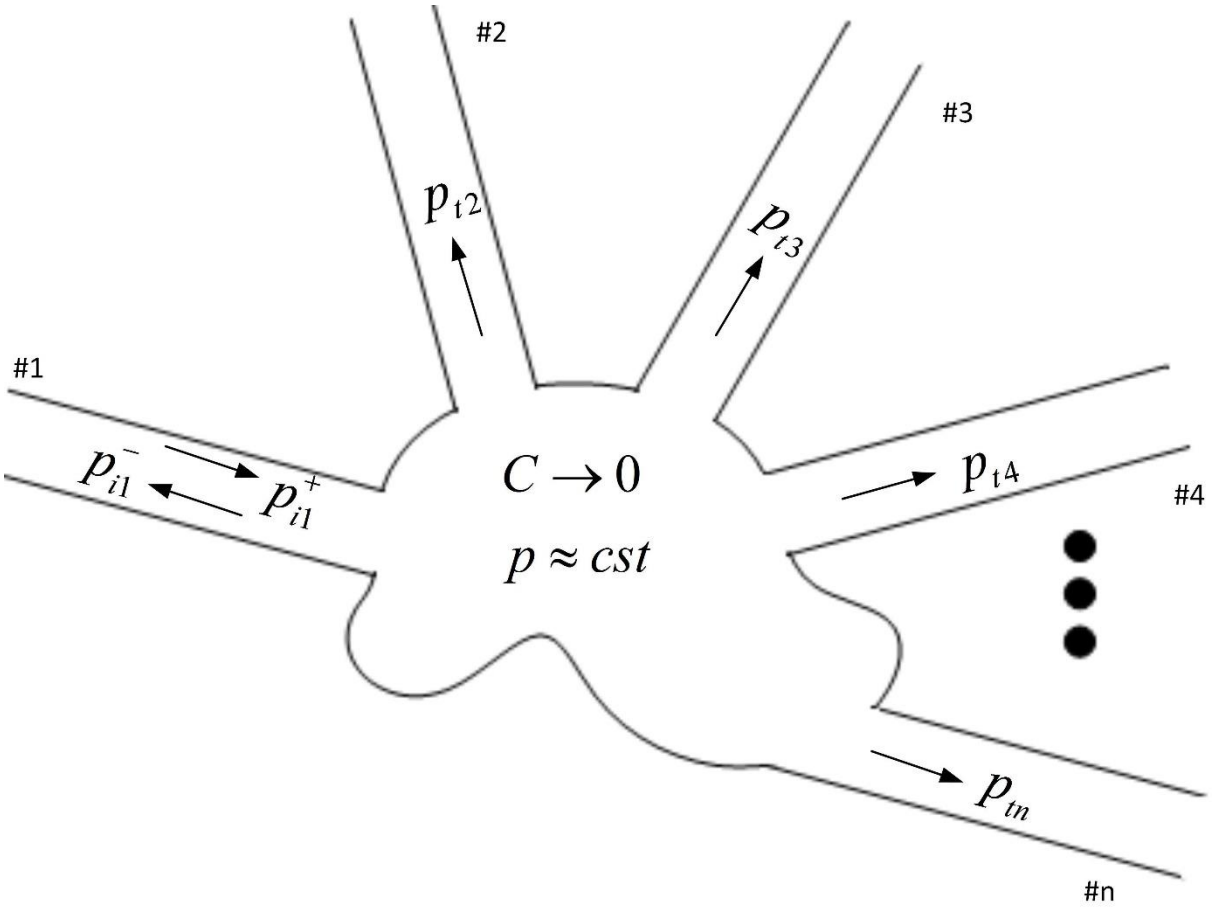

Fig. 5. An arbitrarily-shaped acoustic power divider formed by an intermediate channel having near-zero compressibility. The material property of the channel results in a quasi-static acoustic field, having uniform pressure everywhere. When the channels meet the matching conditions, the input power is completely transmitted and split among the outputs.

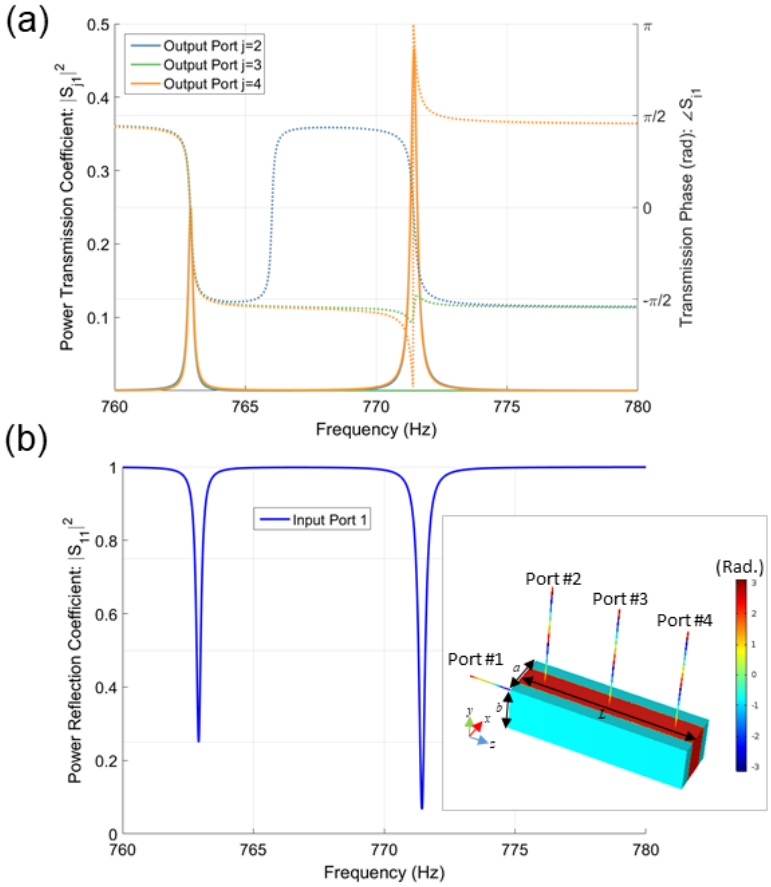

Fig. 6. The geometrical configuration and phase distribution of the uniform-phase equal-amplitude acoustic power divider (*inset-bottom-right*). The system is composed of hard-walled cylindrical waveguides for the input (port #1) and outputs (port #2-4), connected to an intermediate hard-walled channel with rectangular cross section. Operated at its second cut-off frequency, the intermediate channel performs as an effective CNZ medium and results in uniform-phase output signals. Moreover, equal cross-sectional areas of the output waveguides results in equal distribution of output power among them (a) Power transmission coefficient and phase show that the power is divided evenly ($|S_{j1}|^2$=0.25 where $j \in [2,4]$) with equal phase among three output ports at the CNZ frequency of 763 Hz. (b) Power reflection coefficient reveals that we observe nonzero reflection at the input port ($|S_{11}|^2$=0.25 at 763 Hz) and therefore not all of the power is transmitted. The dimensions of the CNZ channel are a=0.450m, b=0.382m, and L=1.5m. The radius of the input/output channels are $r_i = r_o$ =6.3mm.

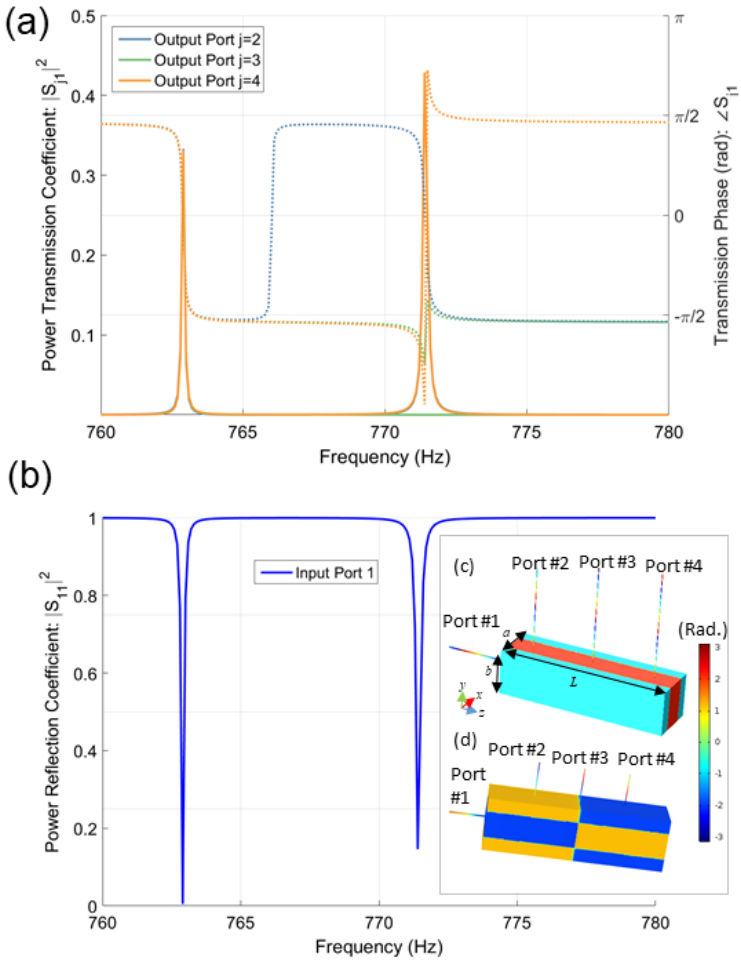

Fig. 7. The power divider of Fig. 2 is modified such that the cross-sectional area of the input waveguide is equal to the sum of the cross-sectional areas of the output waveguides (r_i=6.3mm, $r_o=6.3/\sqrt{3}$ mm). (a) The input signal is split evenly ($|S_{j1}|^2=0.\overline{3}$) and with the same phase among the three output ports at the CNZ frequency of 763 Hz. (b) The reflected power at the CNZ frequency has now been completely suppressed due to the matching condition, dictated by Eq. (25). (c) Spatial phase distribution at the CNZ frequency, showing the uniformity of the phase of the delivered output signals and the geometrical parameters (which are similar to Fig. 2) (d) Spatial phase distribution for the higher-order mode at 773 Hz.

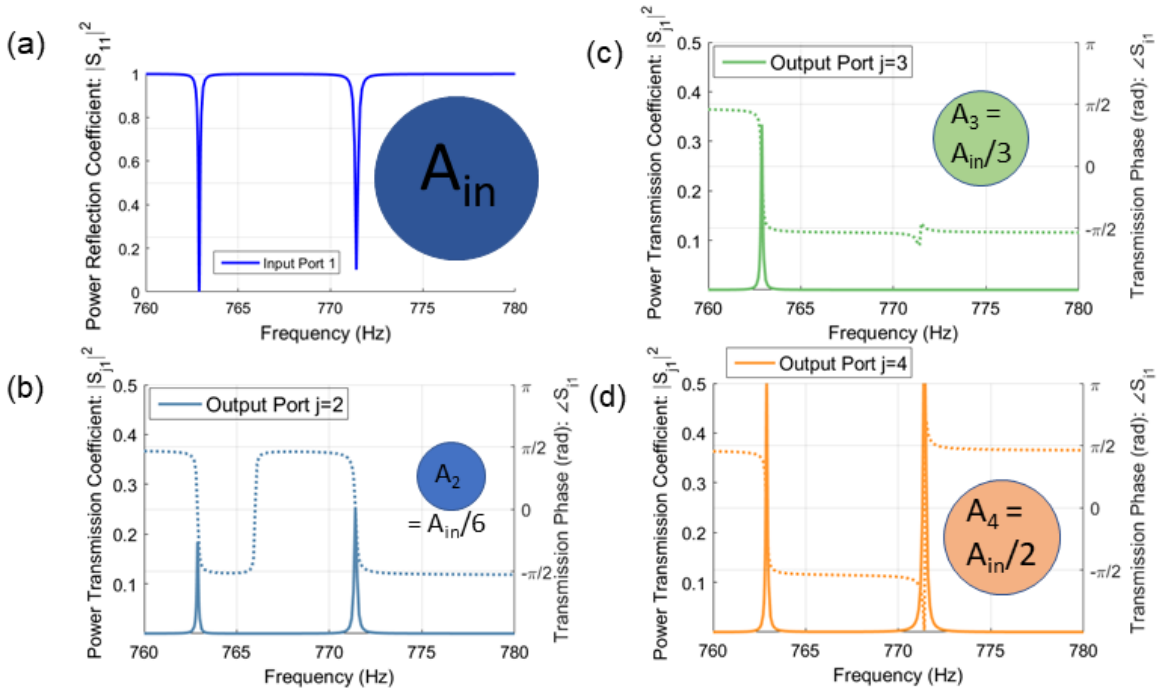

Fig. 8. The matching condition for the input/output waveguides in the power divider, Eq. (25), is met with unequal cross-sectional areas at each output, which allows zero reflection at the input as well as control over the power supplied to each output port. The geometrical parameters of the power divider are similar to Fig. 2 except for the cross-sectional areas of each input/output waveguide, which are indicated by the proportionally-scaled insets in all plots (r_i=6.3 mm, $r_{o2}=6.3/\sqrt{6}$ mm, $r_{o3}=6.3/\sqrt{3}$ mm, $r_{o4}=6.3/\sqrt{2}$ mm). (a) As the matching condition of Eq. (25) is satisfied, the reflected power remains zero at the CNZ frequency of 763 Hz. (b) The cross-sectional area of the second output port is $A_2 = A_{in}/6$ and the output power is $|S_{21}|^2 = 1/6$. (c) $A_3 = A_{in}/3$ and $|S_{31}|^2 = 1/3$. (d) $A_4 = A_{in}/2$ and $|S_{41}|^2 = 1/2$.

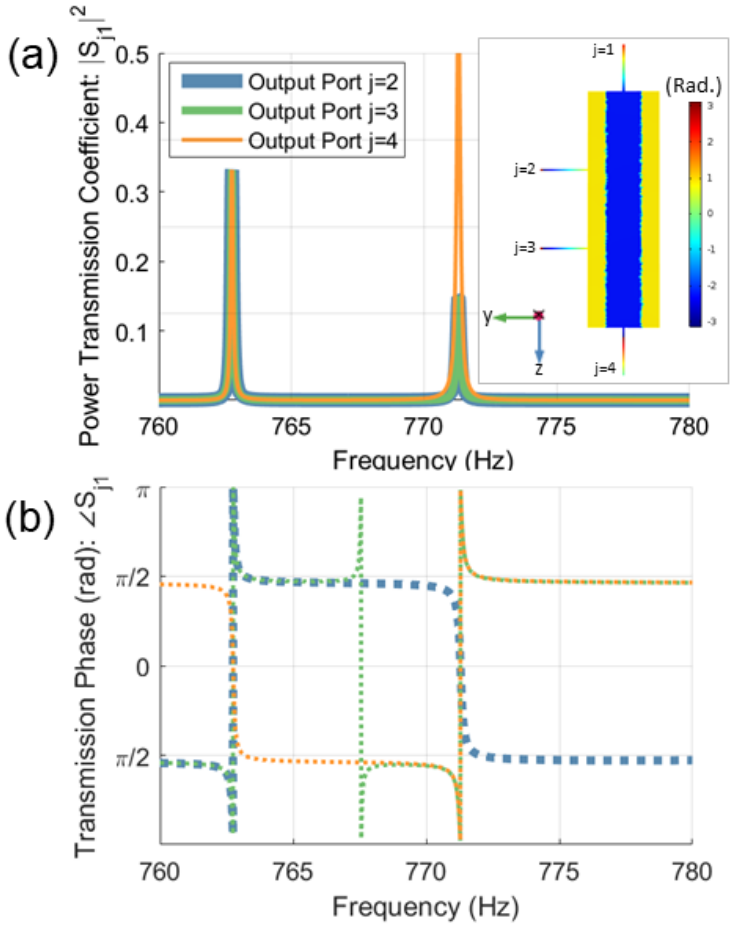

Fig. 9. The geometrical parameters of the power divider are kept identical to Fig. 2, except that the power divider's output ports 2 and 3 are placed along the side of the intermediate channel, while port 4 is placed at the end (see spatial phase profile, *top-right inset*). (a) Power is evenly divided among the three output channels at the CNZ frequency of 763 HZ. (b) At this frequency, the phase is flipped by 180 degrees at the output of both side channels, while the phase is 0 degrees at the interface of port 4.

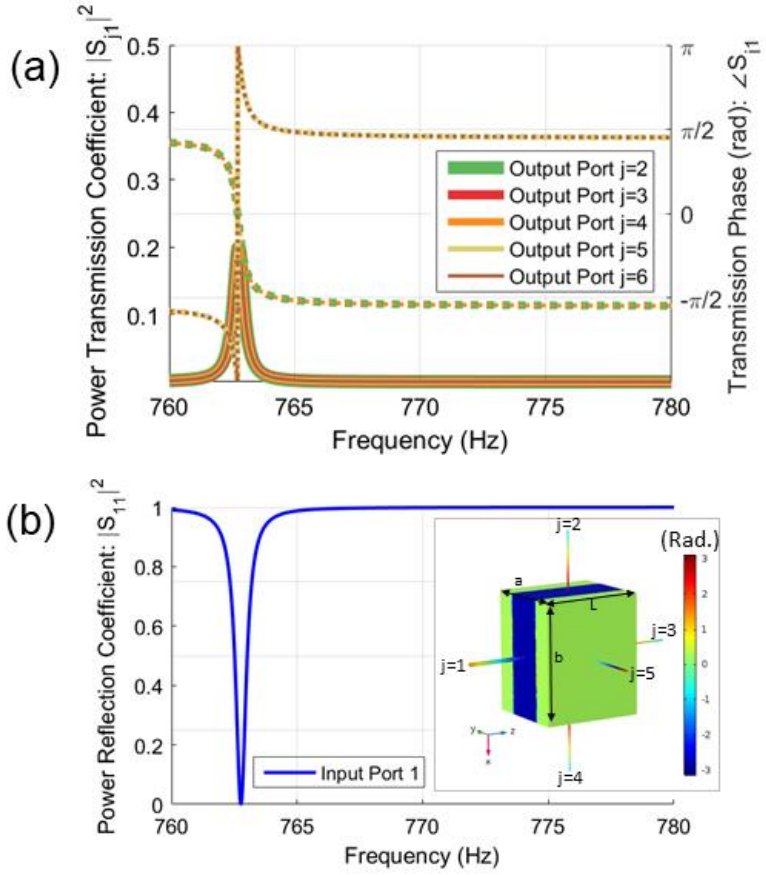

Fig. 10. A more general case of the uniform-phase acoustic power divider, in which the height and length of the channel are varied. This example has a total of 5 output ports (one on each opposing face of the intermediate channel). The power divider maintains uniform phase for any port placed within $\lambda/4$ of the center of the channel and the output phase flips by 180 degrees for any output waveguide that is placed elsewhere (see *inset-bottom*). (a) Power is divided evenly among the 5 output ports at the CNZ frequency of 763 Hz. The phase is zero at the CNZ frequency for ports 2, 3, and 4, and the phase is 180 degrees for ports 5 and 6. (b) The reflected power remains zero at the CNZ frequency. The dimensions are a=0.450m, b=0.6m, L=0.5 m, r_i=6.3mm, and $r_o=6.3/\sqrt{5}$ mm.

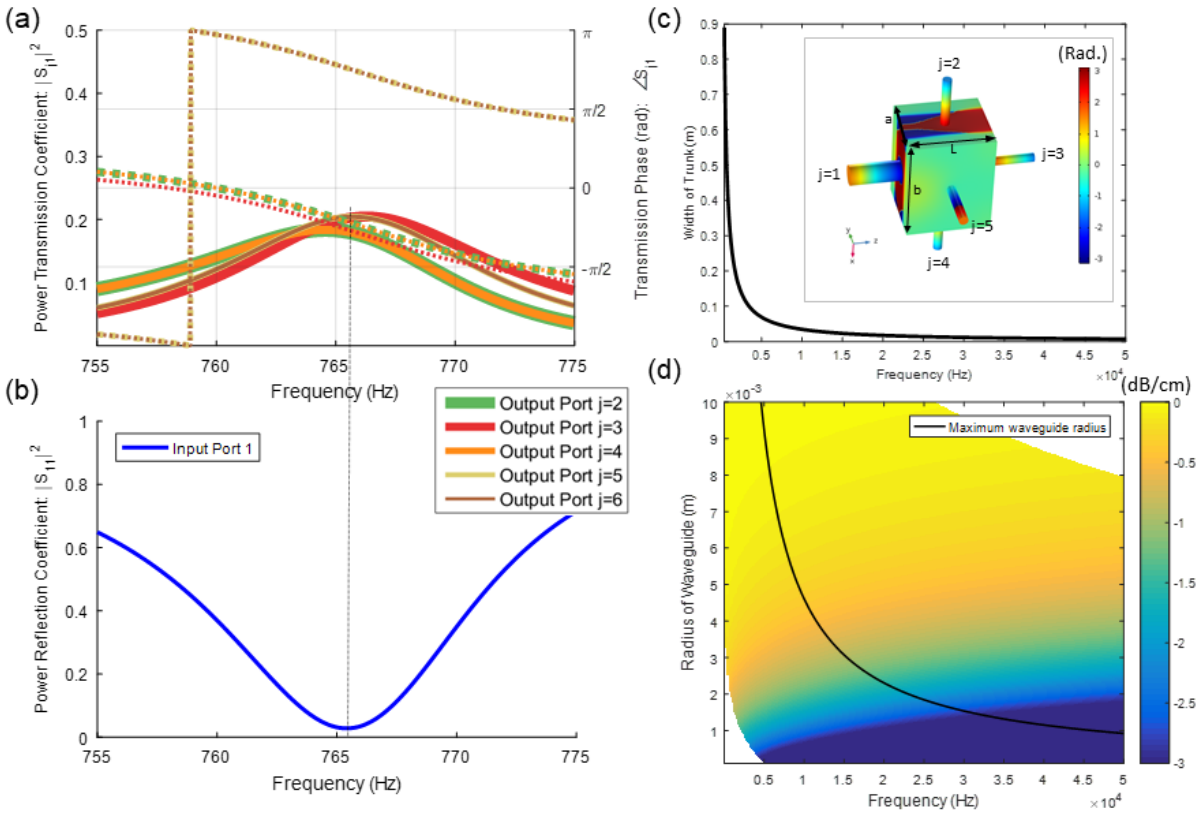

Fig. 11. Scaling limitations for the acoustic power divider. Increasing the size of the input waveguide results in a channel that no longer has uniform phase and the power division becomes uneven. (a) Power transmission coefficients (left axis, solid lines) and phase (right axis, dashed lines) for ports 2-6 when the radius of the input waveguide is $a/8$, where a=0.450m is the width of the intermediate channel. Note that peak power division no longer occurs at the same frequency for each port, although the output power varies by a maximum of 11.5% in this case. The output transmission phase along the central ports (j=2,3,4) has increased from zero in the previous case (Fig. 6) to $\sim \pi / 4$ and varies by a maximum of 0.15 rad. (b) Power reflection coefficient for an input waveguide radius of $a/8$, which has been degraded to 0.03 (compared to the 0 power reflection coefficient of Fig. 10) (c) Variation of the CNZ frequency for a hard-hard channel (where uniform-phase power division can be achieved) as a function of the width of the channel, a. (d) Visco-thermal acoustic boundary layer loss as a function of frequency and waveguide radius. The black curve represents the limit where input radius reaches to $a/8$. Below the black curve, all

choices of radius and frequency can result in power dividers with approximately uniform phase and equal power splitting. Note the units of loss are dB/cm as we are interested in centimeter-scale devices.

References

[1] Engheta, N., Pursuing near-zero response. *Science* **340**, 286-287 (2013).

[2] Ziolkowski, R. W., Propagation in and scattering from a matched metamaterial having a zero index of refraction. *Phys. Rev. E* **70,** 046608 (2004).

[3] Xu, Y., & Chen, H., Total reflection and transmission by epsilon-near-zero metamaterials with defects." *Appl. Phys. Lett.* **98,** 113501 (2011).

[4] Silveirinha, M.G., & Engheta, N., Tunneling of electromagnetic energy through subwavelength channels and bends using epsilon-near-zero materials. *Phys. Rev. Lett.* **97,** 157403 (2006).

[5] Liu, R., Experimental demonstration of electromagnetic tunneling through an epsilon-near-zero metamaterial at microwave frequencies. *Phys. Rev. Lett.* **100,** 023903 (2008).

[6] Edwards, B., Alù, A., Young, M.E., Silveirinha, M.G., & Engheta, N., Experimental verification of epsilon-near-zero metamaterial coupling and energy squeezing using a microwave waveguide. *Phys. Rev. Lett.* **100,** 033903 (2008).

[7] Edwards, B., Alù, A., Silveirinha, M., & Engheta, N., Reflectionless sharp bends and corners in waveguides using epsilon-near-zero effects. *J. Appl. Phys.* **105,** 044905 (2009).

[8] Silveirinha, M.G., & Engheta, N., Theory of supercoupling, squeezing wave energy, and field confinement in narrow channels and tight bends using epsilon-near-zero metamaterials. *Phys. Rev. B* **76,** 245109 (2007).

[9] Alù, A., Silveirinha, M.G., & Engheta, N., Transmission-line analysis of epsilon-near-zero-filled narrow channels. *Phys. Rev. E* **78,** 016604 (2008).

[10] Marcos, J.S., Silveirinha, M.G., & Engheta, N., μ-near-zero supercoupling. *Phys. Rev. B* **91,** 195112 (2015).

[11] Liberal, I., & Engheta, N., Near-zero refractive index photonics. *Nat. Photonics* **11,** 149-158 (2017).

[12] Silveirinha, M.G., & Engheta, N. Design of matched zero-index metamaterials using nonmagnetic inclusions in epsilon-near-zero media. *Phys. Rev. B* **75,** 075119 (2007).

[13] Mahmoud, A.M., & Engheta, N. Wave-matter interactions in epsilon-and-mu-near-zero structures. *Nat. Commun.* **5,** 5638 (2014).

[14] Davoyan, A.R., Mahmoud, A.M, & Engheta, N. Optical isolation with epsilon-near-zero metamaterials. *Opt. Express* **21,** 3279-3286 (2013).

[15] Alù, A., & Engheta, N., Light squeezing through arbitrarily shaped plasmonic channels and sharp bends. *Phys. Rev. B* **78,** 035440 (2008).

[16] Argyropoulos, C., Chen, P., D'Aguanno, G., Engheta, N., & Alù, A. Boosting optical nonlinearities in epsilon-near-zero plasmonic channels. *Phys. Rev. B* **85,** 045129 (2012).

[17] Huang, X., Lai, Y., Hang, Z.H., Zheng, H. & Chan, C.T., Dirac cones induced by accidental degeneracy in photonic crystals and zero-refractive-index materials. *Nat. Mater.* **10,** 582-586 (2011).

[18] Liberal, I., Mahmoud, A.M., Li, Y., Edwards, B., & Engheta, N. Photonic doping of epsilon-near-zero media. *Science* **355,** 1058-1062 (2017).

[19] Liang, Z., & Li, J., Extreme acoustic metamaterial by coiling up space. *Phys. Rev. Lett.* **108,** 114301 (2012).

[20] Esfahlani, H., Karkar, S., Lissek, H., & Mosig, J.R. Acoustic dispersive prism. *Sci. Rep.* **6,** 18911 (2016).

[21] Esfahlani, H., Sami K., Lissek, H., & Mosig, J.R. Exploiting the leaky-wave properties of transmission-line metamaterials for single-microphone direction finding. *J. Acoust. Soc. Am.* **139,** 3259-3266 (2016).

[22] Jing, Y., Xu, J., & Fang, N.X. Numerical study of a near-zero-index acoustic metamaterial. *Phys. Lett. A* **376,** 2834-2837 (2012).

[23] Fleury, R., & Alù, A. Extraordinary sound transmission through density-near-zero ultranarrow channels. *Phys. Rev. Lett.* **111,** 055501 (2013).

[24] Ma, H.F., Shi, J.H., Cheng, Q., & Cui, T.J. Experimental verification of supercoupling and cloaking using mu-near-zero materials based on a waveguide. *Appl. Phys. Lett.* **103,** 021908 (2013).

[25] Hao, J., Yan, W., & Qiu, M. Super-reflection and cloaking based on zero index metamaterial. *Appl. Phys. Lett.* **96,** 101109 (2010).

[26] Enoch, S., Tayeb, G., Sabouroux, P., Guerin, N., & Vincent, P. A metamaterial for directive emission. *Phys. Rev. Lett.* **89,** 213902 (2002).

[27] Yu, Y., Shen, L., Ran, L., Jiang, T., Huangfu, J., Kong, J.A. Directive emission based on anisotropic metamaterials. *Phys. Rev. A* **77,** 053821 (2008).

[28] Nguyen, V.C., Chen, L., & Halterman, K. Total transmission and total reflection by zero index metamaterials with defects. *Phys. Rev. Lett.* **105,** 233908 (2010).

[29] Ma, H.F., Shi, J.H., Cai, B.G., & Cui, T.J. Total transmission and super reflection realized by anisotropic zero-index materials. *New J. Phys.* 14, 123010 (2012).

[30] Cselyuszka, N., Sečujski, M., & Bengin, V.C. Compressibility-near-zero acoustic metamaterial. *Phys. Lett. A* **378,** 1153-1156 (2014).

[31] Alù, A., & Engheta, N., Dielectric sensing in epsilon-near-zero narrow waveguide channels. *Phys. Rev. B* **78,** 045102 (2008).

[32] Alù, A., Silveirinha, M.G., Salandrino, A., & Engheta, N. Epsilon-near-zero metamaterials and electromagnetic sources: Tailoring the radiation phase pattern. *Phys. Rev. B* **75,** 155410 (2007).

[33] Cheng, Q., Jiang, W.X., & Cui, T.J. Spatial power combination for omnidirectional radiation via anisotropic metamaterials. *Phys. Rev. Lett.* **108,** 213903 (2012).

[34] Navarro-Cia, M., Beruete, M., Sorolla, M., & Engheta, N. Lensing system and Fourier transformation using epsilon-near-zero metamaterials. *Phys. Rev. B* **86,** 165130 (2012).

[35] Dubois, M., Shi, C., Zhu, X., Wang, Y., & Zhang, X., Observation of acoustic Dirac-like cone and double zero refractive index. *Nat. Commun.* **8,** 14871 (2017)

[36] Esfahlani, H., Lissek, H., & Mosig, J.R., Generation of acoustic helical wavefronts using metasurfaces. *Phys. Rev. B* **95,** 024312 (2017).

[37] Song, B.H., & Bolton, J.S., A transfer matrix approach for estimating the characteristic impedance and wave numbers of limp and rigid porous materials. *J. Acoust. Soc. Am.* **107,** 1131 (2000).

[38] ASTM E2611-09, Standard test method for measurement of normal incidence sound transmission of acoustical materials based on the transfer matrix method. (ASTM International, West Conshohocken, PA, 2009)

[39] Blackstock, D.T., *Fundamentals of Physical Acoustics*. (John Wiley & Sons, Hoboken, N.J, 2001).

[40] A. Lai, K.M. Leong, & T. Itoh, Infinite Wavelength Resonant Antennas with Monopolar Radiation Pattern Based on Periodic Structures. *IEEE Trans. Antennas Propag.* **55**, No. 3 (2007).

[41] A. Lai, K.M. Leong, & T. Itoh, A novel N-port series divider using infinite wavelength phenomena. *IEEE MTTS Int. Microw. Symp.* (IEEE, Long Beach, CA, 2005): pp. 1001-1004.

[42] M.A. Antoniades & G.V. Eleftheriades, A broadband series power divider using zero-degree metamaterial phase-shifting lines. *IEEE Microw. Compon. Lett.* **15**, No. 11 (2005).

[43] A. Lai, K.M. Leong, & T. Itoh, Novel series divider for antenna arrays with arbitrary element spacing based on a composite right/left-handed transmission line. *Microwave Conference*, 2005 European (IEEE, Paris, 2005): vol. 1

[44] H.V. Nguyen & C. Caloz., Tunable arbitrary N-port CRLH infinite-wavelength series power divider. *Electron. Lett.* ***43***, No. 23, pp. 1292 (2007).

[45] W.L. Stutzman & G.A. Thiele, *Antenna Theory and Design* (Wiley, New York, 1998) 2nd ed.

[46] L.E. Kinsler, A.R. Frey, A.B. Coppens, & J.V. Sanders, *Fundamentals of Acoustics*, (John Wiley & Sons, Hoboken, N.J., 1999): 4th ed., pp. 560.

[47] E.I. Alekseev, E.N. Bazarov, V.P. Gubin, A.I. Sazonov, M.I. Starostin, & A.I. Oussov, Recirculating fibre ring interferometer with compensation for losses in the cavity. *Quantum Electron.* **31** 1113 (2001).

[48] H. Haus, *Waves and Fields in Optoelectronics*, (Prentice-Hall, Englewood Cliffs, NJ, 1984): Chapter 7.

[49] Van Doren, T.W., Propagation of Finite Amplitude Sound in Multiple Waveguide Modes. (PhD. Dissertation, 1993).